The Aeronautical Journal (2022), **126**, pp. 2058–2082
doi:10.1017/aer.2022.31

REGULAR PAPER

Experimental analysis of flow instability detection in a centrifugal compressor using variational mode decomposition

W. Wang , H. Zhang , C. Yang*, C. Yang and C. Hu

School of Mechanical Engineering, Beijing Institute of Technology, Beijing 100081, China
*Corresponding Author. Email: yangce@bit.edu.cn

Received: 7 January 2022; **Revised:** 4 March 2022; **Accepted:** 8 March 2022

Keywords: Centrifugal compressor; Dynamic pressure experiment; Flow instability; Nonlinear and non-stationary signal; Variational mode decomposition

Abstract

In centrifugal compressors, the identification of flow instability signals from experiments is a difficult problem owing to the nonlinear and non-stationary characteristics. Otherwise, the complicated asymmetric structure of the volute brings a huge challenge to the evolution and circumferential nonuniformity characteristics of the flow instabilities. This paper presents experimental and numerical investigations on internal flow field to understand the flow instability characteristics in a centrifugal compressor. Considering nonlinear and non-stationary signals, a method based on Fourier-transform and variational mode decomposition was introduced to analyse the flow instability characteristics. The Fourier spectrum results show that at 0.21kg/s of 80krpm, the pressure signal has a noticeable high-frequency fluctuation, which indicates that the compressor enters the flow instability state. The variational mode decomposition results show that before a surge, the compressor experiences different flow instability stages: the RI stage, the coexistence stage of RI and stall, and the stall stage. Moreover, obvious circumferential nonuniformity characteristics of flow instabilities were observed during the throttling process. RI first occurred at the 180° circumferential position and then the stall first appeared in the circumferential range of 60° to 240°. The simulation results that it is because that the asymmetric volute causes the adverse pressure gradient inside the impeller passage and a high-pressure region (120°–240°) at the upstream of the impeller inlet. Under this combined action of the two, the effect region of tip leakage vortex expands the upstream of the impeller inlet. Meanwhile, the tip leakage vortex core migrates to a lower span of blades. This study demonstrates the ability to analyse nonlinear and non-stationary signals from a centrifugal compressor via variational mode decomposition, and provides a useful guidance for the identification of flow instability signals.

Nomenclature

θ	Circumferential angle
k	Number of decomposed modes
p	Static pressure
f	Frequency
rot	Rotor
t	Time
ω_k	Centre frequency
α	Penalty factor
λ	Lagrangian multiplication operator
η_e	Energy ratio
η_s	Similarity factor
BPF	Blade pass frequency
EMD	Empirical mode decomposition

HHT	Hilbert–Huang transform
L	Extended Lagrange expression
IMF	Intrinsic mode function
RI	Rotating instability
RF	Rotational frequency
VMD	Variational mode decomposition
$H(\omega, t)$	Hilbert amplitude spectrum
$h(\omega)$	Hilbert marginal spectrum
$u_k(t)$	Each decomposed IMF
$z_k(t)$	Analytic signal
$\phi_k(t)$	Instantaneous phase

1. Introduction

Nowadays, turbomachines play a significant role in industrial installations, such as power plants, compressed air energy storage, automotive vehicles and small aircraft. Generally, turbomachines are grouped into two categories. One mainly includes the steam and turbines, which are used to produce power. The other group comprises machines that are used to increase the flow fluid pressure, such as compressors, pumps and fans. The compressor may suffer from different flow instabilities under a low mass flow rate. These type flow phenomena, such as stall and surge, have been investigated through experiments and numerical simulations by several researchers.

Surge is a global, large-amplitude flow oscillation in the compressor system, which causes a loud noise and mechanical vibration. Most notably, surge is a low-frequency and axisymmetric flow. Unlike surge, the rotating stall is a local and circumferential flow disturbance. This phenomenon exists widely in both axial and centrifugal compressors. When a compressor enters rotating stall, the rotating cell propagates from blade to blade at some frequency, loading and unloading each blade. Many researchers have recognised two types of stall inception: spike and modal wave inception [1, 2]. The modal wave is a small amplitude and low frequency disturbance. Greitzer et al. [3] used the Moore-Greitzer model to experimentally investigate modal oscillation behaviour. Based on fast wavelet analysis, Liu et al. [4] achieved low-frequency reconstruction and detected modal wave inception at 110 revolutions before stall in an axial compressor. Arshad et al. [5] reported that modal waves were related to the separation flow near the hub region, whereas they were not related to the origin of the stall disturbance location. Vo et al. [6] summarised two criteria for judging the occurrence of spike-type stall: the spillage and the backflow of tip leakage flow occurs at the blade leading edge and trailing edge, respectively.

For centrifugal compressors, researchers have done many studies on the causes of and location of stall inception. Spakovszky et al. [7] observed that the spike-type stall occurred the in the vaneless space between the impeller and vane diffuser. Everitt et al. [8] revealed that vortical structures increased diffuser inlet blockage and triggered short-wavelength stall in an isolated diffuser. Bousquet et al. [9, 10] found a modal wave stall inception in a centrifugal compressor with a vane diffuser (without a volute). They suggested that the stall wave can propagate upstream and interact with the flow structure at the impeller inlet. Owing to the complex inlet bent torsional pipes and volute structure, the internal flow field become more complicated, thereby affecting the initial occurrence position of stall. Yang et al. [11–13] conducted a lot of experimental and numerical studies on the stall in a centrifugal compressor with a volute. They suggested that volute tongue induced an adverse pressure wave, and the wave propagated backwards into a certain circumferential position at the impeller inlet. The stall first occurred at this position. Zhang et al. [14] summarised the influence of inlet and outlet asymmetric structure on flow field distortion, and they suggested that the compressor stability was reduced when the high static pressure region induced by the inlet bent torsional pipe was located at the same circumferential positions of the high static pressure region induced by the volute.

Apart from surge and rotating stall, rotating instability (RI) is another focus of the flow instability. Kameier et al. [15, 16] suggested that RI can be decomposed by the spatial Fourier transform. RI only

https://doi.org/10.1017/aer.2022.31 Published online by Cambridge University Press

appears when there were a reverse flow in the blade gap. Mailach et al. [17, 18] found that blade tip vortices caused RI. Vo et al. [19] suggested that the RI was due to flow oscillations caused by the tip clearance backflow. Based on acoustic measurements, Sun et al. [20] found that there were four instability phenomena in a centrifugal compressor: rotating stall, RI, mild and deep surge. Li et al. [21, 22] suggested that surface feature was related to the RI behaviours. For a transonic axial compressor, Ye et al. [23] investigated the origin and propagation of RI and discussed the influence of circumferential casing grooves on this instability phenomenon. Zou et al. [24] experimentally investigated the dynamic pressure for two types of centrifugal compressors. At low and middle speeds, the RI was not almost affected by diffuser vanes. In addition, He [25] also adopted a casing treatment to eliminate the rotating instability. For a transonic rotor, Wang et al. [26] revealed the RI phenomenon with a circumferential propagation "multi-passage structure." The RI appeared at the rotor tip region when the compressor operates in the stable range. Other studies [27–30] also have shown the relation between tip leakage flow and RI.

Numerous experiments have indicated that flow instabilities can significantly decrease the performance and operating range of compressors. Therefore, it is necessary to detect the pressure signal from compressor experiments under different operating conditions effectively and quickly. Researchers have used different methods for instability detection, such as time series analysis, time and spatial Fourier transform, and time-frequency analysis methods including short time Fourier transform and wavelet transform. Time series analysis can only study the time domain characteristics of signals, and the Fourier transform can only study the frequency characteristics. The temporal and spatial characteristics of instability signals has been conveniently obtained using a time-frequency method. The one-dimensional continuous wavelet transform has been utilised in studies on compressor stall [31, 32]. Cameron et al. [33] employed different techniques to investigate two representative stall inception events, and they also proposed a windowed correlation technique for the signal detection. For a low-speed contra rotating axial flow fan, Toge et al. [34, 35] studied the stall inception mechanism from unsteady flow measurements using the wavelet transform. Recently, Liu et al. [36] employed various techniques to investigate stall warnings, such as root mean square, auto-correlation, cross-correlation, and fast wavelet analysis. Champ et al. [37] suggested that wavelet analysis and short-time Fourier transform can effectively detect incipient surge conditions. Li et al. [38] also adopted the wavelet transform technique to divide the rotating stall process into RI and stall inception. Moreover, Li et al. [39] and Manas et al. [40, 41] also employed the discrete spatial Fourier series or wavelet transform to study the aerodynamic stability of compressor. Wang et al. [42] observed the RI using the wavelet features.

Recently, novel nonlinear analysis methods have developed rapidly, and can give a better choice to decompose nonlinear signals. Huang et al. [43] proposed creatively a revolutionary time-frequency method called the Hilbert-Huang transform (HHT) combining the empirical mode decomposition (EMD) with Hilbert transform. By this method, a non-stationary and nonlinear signal was be decomposed into different intrinsic mode functions (IMFs), which is an appropriate method for a pressure signal measurement of a compressor, various types of instability signals are typically nonlinear and non-stationary. Li et al. [44] employed the HHT method based on EMD and obtained IMFs in different frequency bands, which can be used to detect aerodynamic instability. Wu et al. [45] suggested that the EMD technique can discover the compressor surge earlier than the Morlet continuous wavelet transform. Zhao et al. [46] employed this method to show the propagation from the normal condition to spike-wave stall inception. Liu et al. [47] proposed a method, namely EEMD, which combines an improved multi-scale fuzzy entropy with an improved EMD, to investigate unstable operating states of a centrifugal compressor. Guan et al. [48] applied the EMD to observe the compressor stall mode. Yue et al. [49] proposed a novel technique which combines an EMD with a local mean decomposition technique. They applied it to investigate the stall data which is nonlinear and non-stationary. However, EMD has shortcomings, such as the mode mixing and the insufficiency of the mathematical theory. Recently, based on variational theory, Dragomiretskiy [50] proposed a new, non-recursive, adaptive technique which is called variational mode decomposition (VMD), to overcome these drawbacks. Compared with EMD, VMD has a strict mathematical theory. Specifically, it is an appropriate approach

https://doi.org/10.1017/aer.2022.31 Published online by Cambridge University Press

for investigating nonlinear and non-stationary signals. Therefore, for compressors operating in an unstable operating range, the VMD method can be considered an effective means to investigate the nonlinear characteristics. In addition, some novel methods were introduced to analyse the flow field in compressors such as dynamic mode decomposition [51] and global stability approach [52].

Most studies have applied traditional methods to study flow instability. However, it is necessary to apply more advanced signal techniques to investigate the instability owing to the presence of the nonlinear and non-stationary characteristics of the signal. The current study aimed to investigate the evolution and circumferential nonuniformity characteristics of flow instabilities under various operating points at 80krpm for a vehicle centrifugal compressor. The study was conducted in the following order:

(1) For a centrifugal compressor with a volute, a dynamic pressure experiment was carried out to obtain the dynamic pressure signals from the near choke to surge.
(2) Fourier transform and VMD methods were used to detect the stable and unstable conditions of the compressor, respectively. The flow instability process was investigated in detail using Hilbert marginal spectrum.
(3) The circumferential nonuniformity phenomenon of flow instability is discussed using unsteady simulations.

2 Brief description of VMD

In this study, VMD technique was adopted to extract the corresponding sub-signals from a pressure signal. VMD could decompose a multicomponent signal into a series of sub-signals. Every sub-signal (IMF) is an amplitude-modulated and frequency-modulated, which can be constructed as follows:

$$u_k(t) = A_k(t)\cos\left(\phi_k(t)\right) \tag{1}$$

where $\phi_k(t)$ is a non-decreasing function and $A_k(t)$is the instantaneous amplitude. For each mode, it is assumed to be compacted mostly around the corresponding centre frequency ω_k.

Based on a Hilbert transform, the analytic signal of each IMF is acquired, and its unilateral frequency spectrum is obtained as follows:

$$\left[\delta(t) + \frac{j}{\pi t}\right] * u_k(t) \tag{2}$$

where $\delta(t)$is the Dirichlet function.

For each mode, an exponential term$e^{-j\omega_k t}$is used to shift the frequency spectrum of the analytic signal to the base band:

$$\left\{\left[\delta(t) + \frac{j}{\pi t}\right] * u_k(t)\right\} e^{-j\omega_k t} \tag{3}$$

A constrained variational problem is constructed as follows:

$$\begin{cases} \min\limits_{\{u_k\},\{\omega_k\}} \left\{ \sum\limits_{i=1}^{K} \left\| \partial_t \left\{ \left[\delta(t) + \frac{j}{\pi t}\right] * u_k(t) \right\} e^{-j\omega_k t} \right\|_2^2 \right\} \\ \text{s.t.} \sum\limits_{i=1}^{K} u_k(t) = x(t) \end{cases} \tag{4}$$

Where $\{u_k\} := \{u_1, \ldots, u_K\}$ are the modes, and $\{\omega_k\} := \{\omega_1, \ldots, \omega_K\}$ are the corresponding centre frequencies, respectively.

The solution method is to convert this constrained problem into the unconstrained variation problem; therefore, VMD introduces the penalty factor α and Lagrangian multiplication operator λ. The extended

https://doi.org/10.1017/aer.2022.31 Published online by Cambridge University Press

Lagrange expression is the following formula:

$$L\left(\{u_k\},\{\omega_k\},\lambda\right)=\alpha\sum_{i=1}^{K}\left\|\partial_t\left\{\left[\delta(t)+\frac{j}{\pi t}\right]*u_k(t)\right\}e^{-j\omega_k t}\right\|_2^2+\left\|f(t)-\sum_{k=1}^{K}u_k(t)\right\|_2^2+\left\langle\lambda(t),f(t)-\sum_{k=1}^{K}u_k(t)\right\rangle \tag{5}$$

The alternate direction method of multipliers (ADMM) is adopted to iteratively find the solution to the saddle point of the L. More details about the ADMM algorithm are provided in Ref. (50). VMD can effectively deal with a complex, nonlinear and multicomponent signal. Each sub-signal or IMF has a very limited bandwidth and is around its corresponding characteristic centre frequency ω_k. In addition, the effect of the VMD method is strongly associated with the two key parameters, penalty factor α and mode number K. Therefore, one of main purpose in next section is to investigate how to obtain the optimal parameters for effective decomposition.

3 Selection of the key parameters and method validation

The mode number K represents the number of sub-signals into which the origin signal has been decomposed. The penalty factor α is related to the mode bandwidth and data fidelity, also called the balancing parameter. These two parameters affect the decomposition effect of the VMD method. Depending on whether the mode number is small or large, the results can be either under or over decomposed. These two important variables must be defined in advance when the VMD is employed to process a complex compound signal.

Before using the VMD method to decompose dynamic experiment signals, both parameters K and α must be defined. The effect of these two parameters was investigated by designing a multicomponent compressor signal $x(t)$ at 80krpm. The input signal included typical compressor frequency components, namely the blade passing frequency (BPF), rotation frequency (RF), RI frequency, spike-wave stall frequency, modal-wave stall frequency, rotor frequency and surge frequency. The sampling frequency f_s for the simulation signal was 200kHz. The signal $x(t)$ and each sub component are expressed in Equations (6)–(12), and illustrated in Figs. 1 and 2.

$$x_1=100\cos(2\pi f_{\mathrm{BPF}}t) \tag{6}$$

$$x_2=50\sin(2\pi f_{\mathrm{RI}}t) \tag{7}$$

$$x_3=30\cos(2\pi f_{\mathrm{rot}}t) \tag{8}$$

$$x_4=150\sin(2\pi f_{\mathrm{spike}}t) \tag{9}$$

$$x_5=150\sin(2\pi f_{\mathrm{modal}}t) \tag{10}$$

$$x_6=250\mathrm{sins}(2\pi f_{\mathrm{surge}}t) \tag{11}$$

$$x(t)=x_1+x_2+x_3+x_4+x_5+x_6 \tag{12}$$

where $f_{\mathrm{BPF}}=9{,}333.33\mathrm{Hz}$, $f_{\mathrm{RI}}=4{,}666.67\mathrm{Hz}$, $f_{\mathrm{rot}}=1{,}333.33\mathrm{Hz}$, $f_{\mathrm{spike}}=800\mathrm{Hz}$, $f_{\mathrm{modal}}=266.67\mathrm{Hz}$, and $f_{\mathrm{surge}}=66.67\mathrm{Hz}$.

Different parameter combinations were selected to study the effect of these two parameters on the decomposition effect. Owing to large quantities of sampled data, the time-domain diagram of each component is unclear, therefore, only the frequency spectrum of each component was displayed after VMD. Figure 3 shows the frequency spectra of the decomposition results at $k=5$, which is less than the number of original signal components. When penalty factor α is very small ($\alpha=0.01\,f_s$), it can be observed that there is a frequency component of 266.67Hz in IMF4 and IMF5. Multiple components of the signal

https://doi.org/10.1017/aer.2022.31 Published online by Cambridge University Press

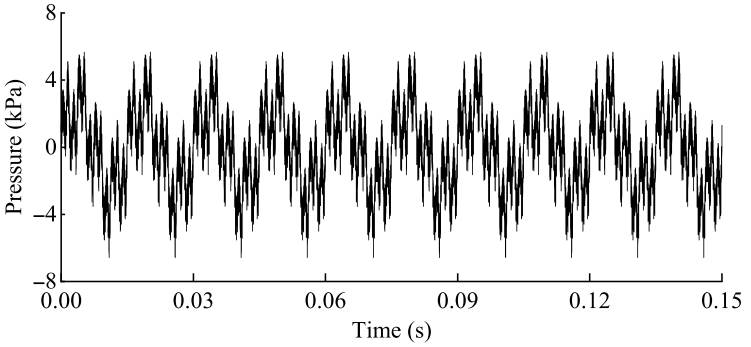

Figure 1. *Simulation signal x(t).*

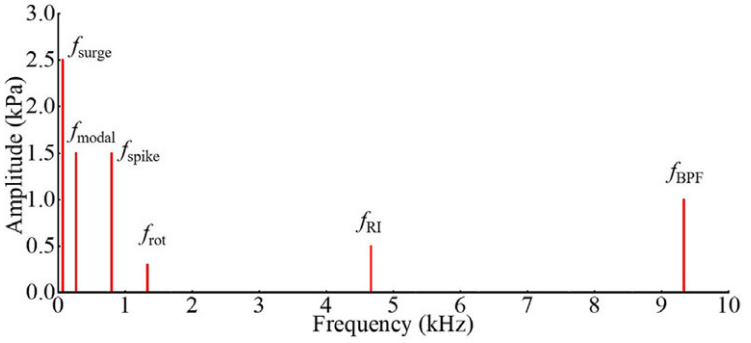

Figure 2. *Frequency spectrum of simulation signal x(t).*

appear in an IMF simultaneously. When the penalty factor α is extremely large ($\alpha = 4f_s$), it can be found that the component with the frequency of 4,666.67Hz is discarded.

Figure 4 shows the frequency spectra of the decomposition results at $k = 6$, which is the number of original signal components. The penalty factor α is set to $0.01f_s$, $0.3f_s$ and $10f_s$. At $\alpha = 0.01f_s$, it can be observed that the component with the frequency component of 266.67Hz is decomposed into IMF5 and IMF6. At $\alpha = 0.3f_s$, it is obvious that the frequency component of each IMF is highly consistent with that of the original signal components. At $\alpha = 10f_s$, the corresponding components of 1,333.33Hz is discarded. The corresponding components of 66.67Hz is decomposed into IMF5 and IMF6.

Figure 5 shows the frequency spectra of the decomposition results at $k = 7$, which is larger than the number of original signal components. When penalty factor α is very small ($\alpha = 0.01f_s$), the component with a frequency of 4,666.67Hz is decomposed into IMF2 and IMF3. When penalty factor α is extremely large ($\alpha = 10f_s$), the component with the frequency of 1,333.33Hz is discarded. Meanwhile, the corresponding components of 800Hz is decomposed into IMF3 and IMF4. The corresponding components of 66.67Hz is decomposed into IMF6 and IMF7.

According to the above analysis, an unreasonable mode number K and penalty factor α will cause a mode mixing problem. Mode mixing indicates that there are several different frequency components in the same IMF, or the same frequency component is shared by several different IMFs and the corresponding centre frequencies coincide, namely mode duplication. In addition to mode mixing, a larger α will cause important information to be missed in the signal decomposition. Therefore, it is necessary to choose the appropriate K and α.

At present, there are many indicators (entropy, energy loss coefficient, and correlation coefficient) in signal analysis; however, using a single indicator to measure signal characteristics is not optimal. Hence, a comprehensive evaluation indicator based on the energy ratio and frequency similarity factor was used to solve this problem, thereby obtaining optimal K and α.

https://doi.org/10.1017/aer.2022.31 Published online by Cambridge University Press

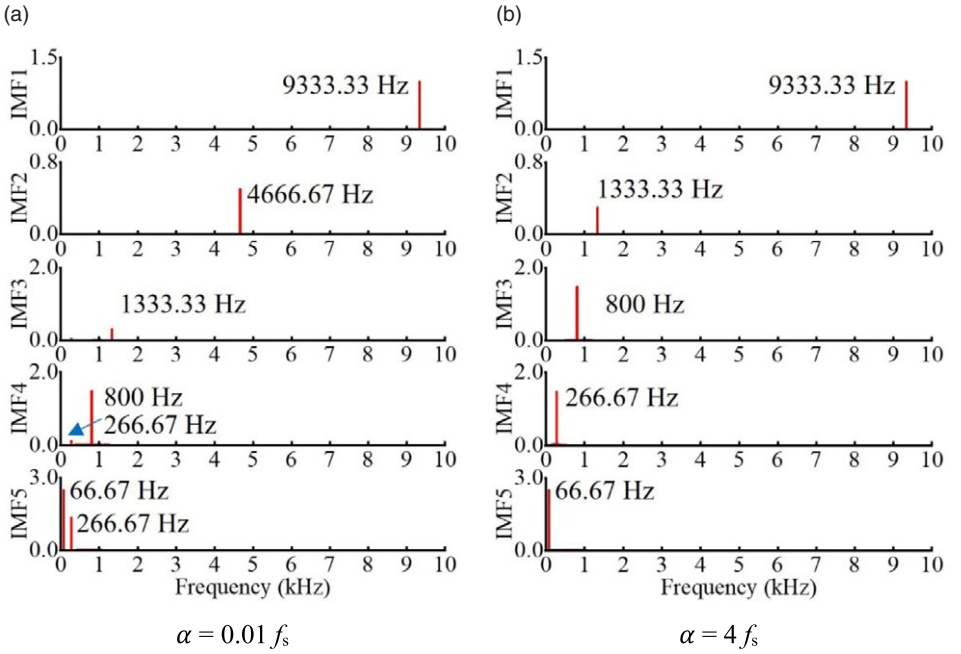

Figure 3. *Decomposition results of VMD at $k = 5$.*

In this study, the energy ratio η_e was considered as the weight of the similarity factor. The indicator is defined as a ratio of the total energies of all the IMFs to the original signal energy, which can be calculated using the following equation:

$$\eta_e = \frac{\sum_{k=1}^{M}\sum_{t=1}^{N}[u_k(t)]^2}{\sum_{t=1}^{N}[x(t)]^2} \tag{13}$$

where $x(t)$, M, and N represents the original signal, the mode number, and the total length of the original signal, respectively. The closer the total energy of all IMF components is to the total energy of $x(t)$, the better the decomposition effect is.

For over-decomposition, some spurious components with a close centre frequency will be generated; however, these modes should belong to the same component. Therefore, a similarity factor used to assess the similarity of adjacent centre frequencies is defined as follows:

$$\eta_s = \frac{\omega_{k+1}}{\omega_k} \tag{14}$$

When the ratio is larger than 0.95, it can be considered that the centre frequency overlaps, which indicates that modal mixing occurs.

Eventually, the operation steps can be summarised as follows:

(1) The modal number K is estimated through the signal Fourier spectrogram and the K range is set.

(2) VMD is performed for the signal.

(3) The energy ratio is calculated and the minimum ratio for the decomposition result for each K is selected.

(4) The similarity factor for the decomposition result of the minimum ratio is calculated to obtain a reasonable decomposition.

https://doi.org/10.1017/aer.2022.31 Published online by Cambridge University Press

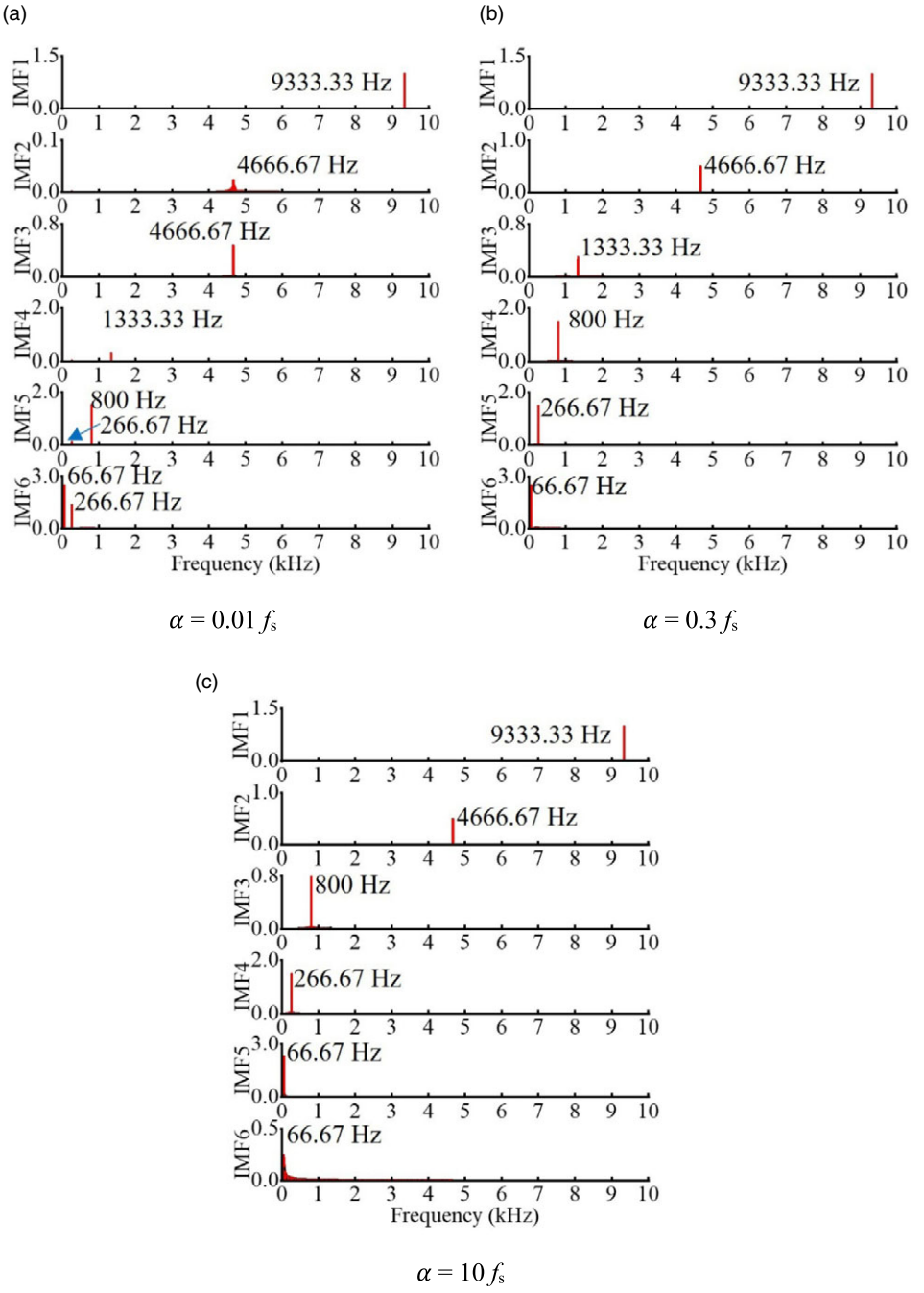

Figure 4. *Decomposition results of VMD at k = 6.*

4 Test facility and numerical method

4.1 Experimental setup

The experiments in this research were performed in the centrifugal compressor with a volute for a vehicle diesel engine. Figure 6 shows the test rig. Figures 7 and 8 show the turbocharger and the centrifugal compressor model, respectively. The compressed air from the air supply drove the turbine,

https://doi.org/10.1017/aer.2022.31 Published online by Cambridge University Press

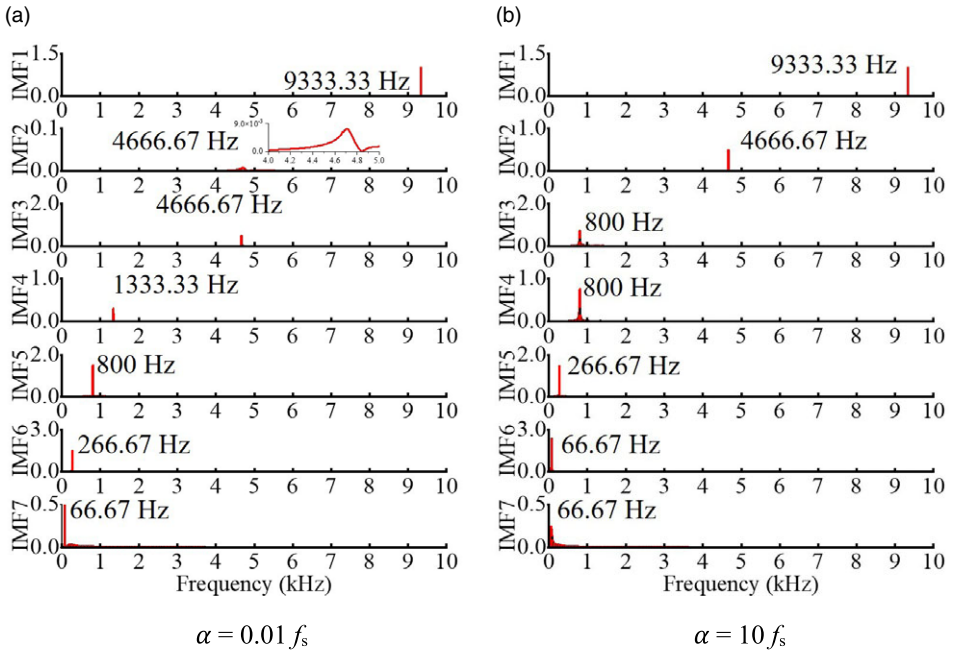

Figure 5. *Decomposition results of VMD at $k = 7$.*

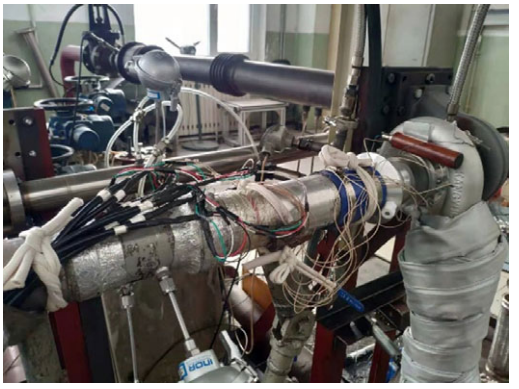

Figure 6. *Schematic diagram for test rig.*

thereby driving the centrifugal compressor. The compressor stage consisted of an inlet pipe, centrifugal impeller, vaneless diffuser, and asymmetric volute. The pressure ratio was 1.92 and the design mass flow rate was 0.26kg/s at the design rotating speed with 90krpm. Table 1 lists more key parameters of the investigated compressor.

4.2 Data acquisition analysis

The experimental measurements included two aspects: the compressor performance and dynamic casing static pressure in the inlet of the impeller. The rotational speed and mass flow rate were collected by an electromagnetic sensor and a lemniscate flowmeter, respectively. At both the inlet and outlet, resistance sensors were used to record the temperature. The Dwyer stainless steel Pitot tube was installed at the compressor inlet and outlet pipes and equipped with the PTX5072-TC-A3-CB-H0-PA (inlet pipe) sensor

https://doi.org/10.1017/aer.2022.31 Published online by Cambridge University Press

Table 1. *Key parameters of investigated centrifugal compressor*

Parameter	Symbol	Value
Number of blades	Z	7 + 7
Leading edge hub radius	r_{1h}	9.35mm
Leading edge shroud radius	r_{1s}	31.4mm
Impeller inlet diameter	D_1	62.8mm
Impeller outlet diameter	D_2	85mm
Diffuser inlet diameter	D_3	96mm
Diffuser outlet diameter	D_4	135mm
Blade backward swept angle	β_{2b}	35°
Tip clearance height	h	0.4mm

Figure 7. *Turbocharger.*

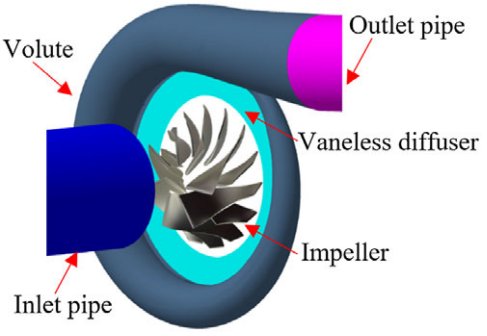

Figure 8. *Centrifugal compressor model.*

and the PTX5072-TC-A3-CA-H0-PA (outlet pipe) sensor to measure the total pressure. The Pitot tube has a diameter of 3.18mm, which is 6.36% of the inlet pipe and 5.3% of the outlet pipe. In this experiment, the compressor flow instability was investigated based on the dynamic casing pressure along a circumference at the impeller inlet. At the impeller inlet, six KULITE XT-140M sensors were used to obtain the dynamic pressure, which were placed evenly and circumferentially around the casing wall. More detailed parameters of KULITE XT-140M are shown in Table 2. Figure 9 illustrates the schematic diagram for the sensor locations, marked with P1–P6.

Compressor speed sweeps (from 70 to 100krpm) were performed from choke to near surge. During this period, the compressor performance characteristics and dynamic static pressure were simultaneously recorded. The compressor could operate at various mass flow rates by adjusting the valve opening.

https://doi.org/10.1017/aer.2022.31 Published online by Cambridge University Press

Table 2. *Main parameters of pressure sensor*

Type	XTE-140 (M)
Pressure range	7 Bar
Operational mode	Absolute
Rated electrical excitation	10 VDC/AC
Natural frequency	380kHz
Operating temperature range	–55°C to +273°C

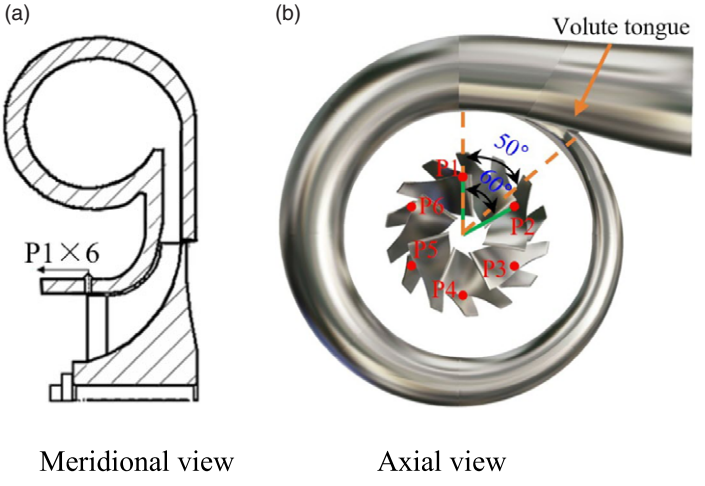

Figure 9. *Schematic diagram for sensor location.*

Figure 10. *Recorded data of the dynamic experiment.*

Each data recording started after the compressor operated stably for a period of time. The pressure data acquisition system records lasted 10s at a sample rate of 200kHz to capture the fully developed instability. The occurrence of low-frequency noise indicated that the compressor has entered a deep surge state. Immediately, the record was stopped and the compressor recovered from the surge by increasing the mass flow quickly to avoid damaging the test rig. The recorded data are shown in Fig. 10.

https://doi.org/10.1017/aer.2022.31 Published online by Cambridge University Press

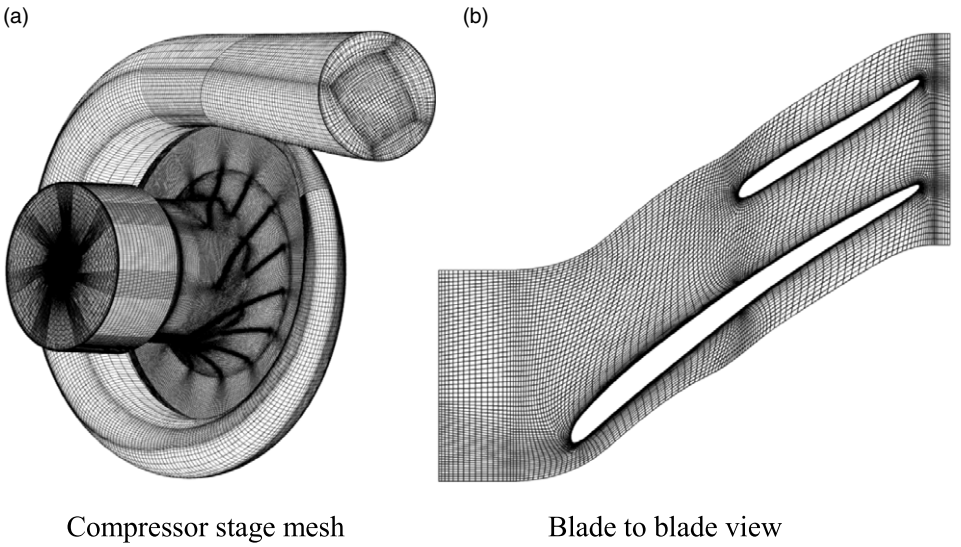

Figure 11. *Centrifugal compressor mesh.*

4.3 Numerical procedure

The flow instability in this centrifugal compressor was accurately captured by conducting a full-annulus 3D unsteady numerical simulation with the EURANUS solver of the commercial software NUMECA. For the unsteady simulation, the 3D Reynolds-averaged Navier–Stokes (RANS) equations were discretised with the dual time-stepping technique temporally and with the cell-centered finite volume technique spatially. The Spalart–Allmaras (SA) one-equation model was employed for turbulence closure. This turbulence model has been validated previously for the investigation on flow instability in centrifugal compressors [53, 54]. At the inlet, the axial flow, total pressure (101,325Pa), and total temperature (298K) were imposed while the average static pressure was applied at the outlet. The flow field results under different operating conditions were obtained by gradually increasing the outlet static pressure. In addition, during a rotating period, the physical time step was set to 280, and 60 inner iterations per time step were adopted for each physical time step.

The computational domains consist of the inlet pipe, centrifugal impeller, vaneless diffuser, volute, and outlet pipe. Significantly, the upstream inlet pipe domain extended to five times the length of the impeller inlet diameter. The downstream outlet pipe domain also extended to five times the length of the volute outlet pipe diameter. Using the module IGG/AutoGrid5, the structured mesh was generated. The rotor/stator interface connection was used between the inlet pipe and the centrifugal impeller, and between the centrifugal impeller and vaneless diffuser. Prior to performing numerical simulations, the grid independence test was verified to guarantee calculation accuracy and save calculation time. Otherwise, this study only focuses on the flow instability at 80krpm; therefore, simulations were carried out only at this speed. To ensure that the simulation results were not related to the grid distribution, three different grid configurations, coarse mesh (8,143,265), medium mesh (8,510,513) and refined mesh (9,417,769) were conducted by adjusting the node distribution in the span and streamwise directions. Considering the pressure ratio and efficiency from steady simulations, it was proven that the medium mesh was already sufficient for obtaining reliable simulation results. Otherwise, the simulation results from the medium mesh were consistent with the experiments, as illustrated in Fig. 12. Eventually, a medium mesh was used in this study. The y+ value was less than five throughout the computational domain, which meets the requirements of the turbulence model. The CFD model could provide reliable evidence for investigating the flow field in future research. Figure 11 shows the centrifugal compressor mesh.

https://doi.org/10.1017/aer.2022.31 Published online by Cambridge University Press

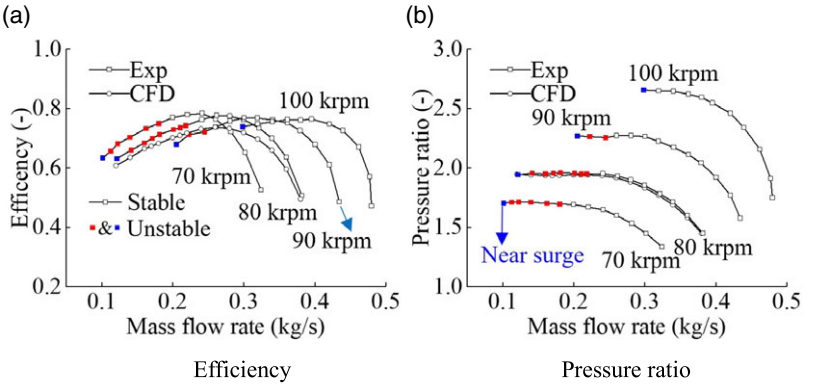

Figure 12. *Performance characteristics of centrifugal compressor.*

5 Compressor performance and CFD validation

Figure 11 shows the compressor performance characteristics under four rotational speeds of 70, 80, 90 and 100krpm. The unstable operating range is marked in red for each rotational speed. The last point represents the near-surge, marked in blue. Significant differences were observed in the instability range of the compressor. At 70krpm, the compressor mass flow rate fluctuates suddenly from approximately 0.19kg/s, although the compressor can still operate normally. The instability flow range accounted for 40.34% of the overall operating range. At 80krpm, the mass flow rate fluctuated from approximately 0.21kg/s, and the instability flow range accounted for 38.46% of the overall operating range. At 90krpm, the mass flow rate fluctuated obviously from approximately 0.25kg/s, and the instability flow range accounted for 19.57% of the overall operating range. At 100krpm, the compressor entered the surge state directly from the stable flow. It can be concluded that the instability range at low speeds is significantly wider than that under high-speed conditions. As illustrated in Fig. 12, it is clear that the compressor experiences different types of work states, including stable and unstable operating conditions (RI, stall, and surge). However, it is difficult to visually distinguish between the types and the development of instability based on experimental data.

6 Compressor instability characteristics and evolution

6.1 Pre-Processing

Before data analysis, the dynamic pressure signals obtained from the experimental measurements must be pre-processed. The dynamic pressure signal can be decomposed into constant and pulsating components. The constant component is very large and produces a large amplitude at 0Hz in the spectrum analysis, obscuring other frequency components. Therefore, the average value must be subtracted from the dynamic pressure data, as shown below:

$$p_{\text{pulsating}} = p_{\text{exp}} - p_{\text{average}} \tag{15}$$

Generally, the BPF component and components less than the BPF are the key research objects. Therefore, it is generally necessary to filter the data to remove the high-frequency components. In this study, the Fourier transform filter is chosen. The low-pass filter blocks all high-frequency components above the BPF and allows only the low-frequency components to pass.

6.2 Instability onset detection based on Fourier transform

The work state of the compressor can be divided into two stages: stable and unstable operating conditions. Under the stable operating conditions, compressor operates well, and there are no strong nonlinear phenomena, such as stall and surge. Therefore, the Fourier transform is sufficient to detect the onset of

https://doi.org/10.1017/aer.2022.31 Published online by Cambridge University Press

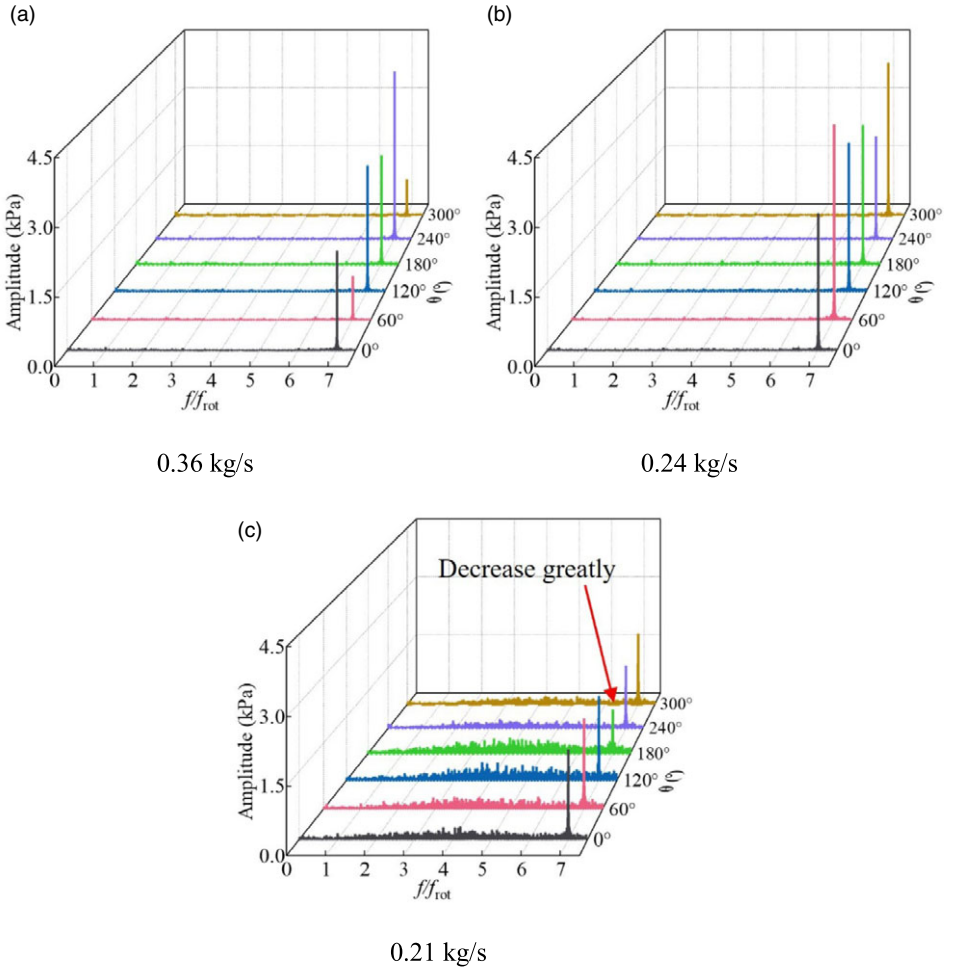

Figure 13. *Frequency spectra at different mass flow rates at 80krpm.*

instability and judge whether the compressor enters an unstable state. Figure 13 shows the frequency spectra of the pressure fluctuation at different circumferential positions from the high mass flow rate point to the low mass flow rate point. The horizontal, longitudinal and vertical axes represent the dimensionless frequencies obtained by dividing the rotor frequency, circumferential angle θ, and static pressure, respectively. The horizontal coordinate 1 represents the RF, whereas 7 represents the BPF. It can be observed that there are almost no significant low-frequency components below BPF under the high mass flow rate (0.36kg/s) and the medium mass flow rate (0.24kg/s) conditions. However, the spectrum characteristics were significantly different at low mass flow rates. At 0.21kg/s, the frequency components below the BPF become very noticeable. The frequency range was mainly concentrated between the 2 RF and BPF. This phenomenon indicates that new and complicated pressure fluctuations occur in the flow field. Therefore, it can be inferred that the compressor entered an unstable working state at the mass flow rate of 0.21kg/s.

6.3 Instability characteristics analysis based on VMD

6.3.1 Comparison of Hilbert marginal spectrum and Fourier spectrum

Before VMD, the mode number can be estimated using the Fourier frequency spectrum of the signal $x(t)$. The number of frequency bands in the spectrum diagram can be used as the initial value for choosing

https://doi.org/10.1017/aer.2022.31 Published online by Cambridge University Press

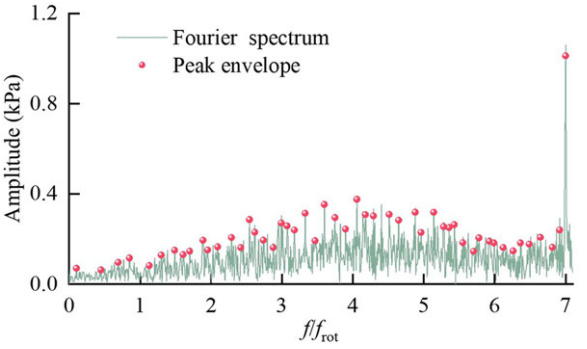

Figure 14. *Frequency spectrum peak envelope at 0.21kg/s, at 80krpm.*

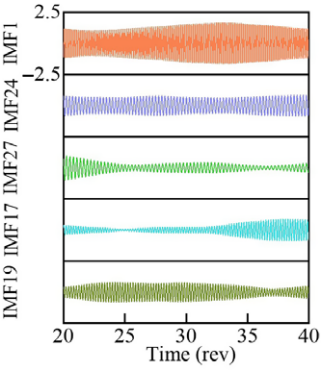

Figure 15. *Decomposition result by VMD.*

the number of decomposition modes by VMD. The amplitude of the BPF component at the 180° circumferential position clearly decreased. Based on the above analysis, the frequency spectrum envelope was extracted at the 180° circumferential position at mass flow rate of 0.21kg/s. As shown in Fig. 14, the local extreme points are marked with a red ball. There were 50 local extreme points; therefore, the initial mode number K was set to 50. The mode number K ranged from 45 to 55. Finally, the optimal K was 50 and the penalty factor was $1.55 f_s$. Owing to the larger number of IMF components, it is difficult to show them all in the figure. Therefore, only the first five IMF components with a larger Fourier spectrum amplitude from the 20th to 40th revolutions and their corresponding Fourier frequency spectrum results are illustrated in Figs 15 and 16. It can also be observed that these IMF components are aperiodic signals with amplitudes varying with time. These IMFs show significant nonlinear and non-stationary characteristics.

When the compressor operates at a low mass flow rate, the flow field becomes unstable and complex, thereby leading to flow instabilities (RI, stall or surge). Moreover, the compressor instabilities exhibits a strong nonlinear process. Therefore, the measured static pressure has strong nonlinear characteristics, such as amplitude, average and standard deviation. The traditional method cannot accurately describe this nonlinear problem. Previously, many researchers have used the Fourier transform to analyse the dynamic experimental data, which is nonlinear and non-stationary. However, Huang et al. [43] argued that the Fourier transform could introduce several additional harmonic components to simulate the non-stationary data owing to the linear superposition of trigonometric functions, which may induce spurious harmonic components. Otherwise, it can be observed that the frequency characteristics of the dynamic pressure data show a multi-peak frequency band. It is not clear which important frequencies

https://doi.org/10.1017/aer.2022.31 Published online by Cambridge University Press

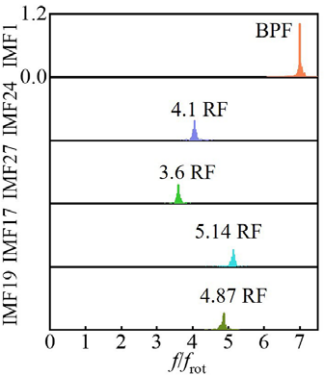

Figure 16. *Fourier spectrum of IMF components.*

dominate during the acquisition time. The VMD method is a new, fully intrinsic and adaptive variational method. This method can adaptively decompose the nonlinear and non-stationary signals into their principal modes (IMFs) with different frequencies. Dragomiretskiy [50] suggested that the proposed VMD method performs clearly better with less spurious components. To avoid the shortcoming of the Fourier transform, Huang introduced the Hilbert marginal spectrum to analyse nonlinear and non-stationary data, which is suitable for the measurement data of the dynamic experiment of the compressor. The Hilbert marginal spectrum approach is defined as follows:

The time-domain signal $x(t)$ is decomposed into a series of IMFs using VMD method:

$$x(t)=\sum_{k=1}^{M} u_k(t) \tag{16}$$

The Hilbert transform result of each IMF u_k can be obtained:

$$H(t)=\frac{1}{\pi}P\int_{-\infty}^{+\infty}\frac{u_k(\tau)}{t-\tau}d\tau \tag{17}$$

where P is Cauchy principal value.

An analytical signal can be constructed as below:

$$z_k(t)=u_k(t)+iH(t)=a_k(t)e^{i\theta_k(t)} \tag{18}$$

$$a_k(t)=\sqrt{u_k{}^2(t)+H^2(t)} \tag{19}$$

$$\theta_k(t)=\arctan\left(\frac{H(t)}{u_k(t)}\right) \tag{20}$$

where $a_k(t)$ and $\theta_k(t)$ represent amplitude and phase.

The instantaneous frequency of each IMFu_k is calculated as follows:

$$\omega_k(t)=\frac{d\theta_k(t)}{dt} \tag{21}$$

After performing the Hilbert transform on each IMF component, the signal $x(t)$ can be expressed in the following form:

$$x(t)=\mathrm{Re}\left(\sum_{k=1}^{M} a_k(t)e^{i\int\omega_k(t)dt}\right) \tag{22}$$

https://doi.org/10.1017/aer.2022.31 Published online by Cambridge University Press

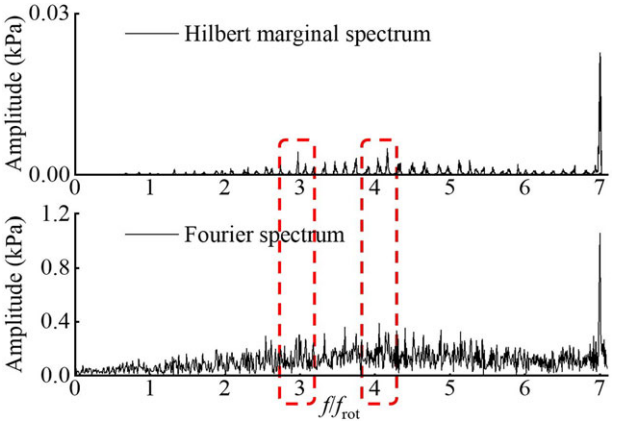

Figure 17. *Comparison between the Hilbert marginal spectrum and Fourier spectrum at 180° circumferential position at 0.21kg/s, 80krpm.*

The equation indicates that the amplitude and instantaneous frequency are expressed as functions of time. The amplitude can be contoured on the frequency–time plane, which is called the Hilbert amplitude spectrum:

$$H(\omega, t) = \mathrm{Re}\left(\sum_{k=1}^{M} a_k(t) e^{i\int \omega_k(t)dt}\right) \tag{23}$$

On this basis, a marginal spectrum was introduced to investigate the instability process. The detailed definition is as follows:

$$h(\omega) = \int_0^T H(\omega, t)dt \tag{24}$$

The Hilbert marginal spectrum is the time-domain integral of the Hilbert spectrum, which depicts the cumulative amplitudes of the whole data. In other words, the Hilbert marginal spectrum offers a measure of the total amplitude contribution from each frequency value. The frequency component with the large cumulative amplitude is dominant in the multicomponent signal. Huang [43] provides more detailed comparisons with the Fourier transform, which shows that the marginal spectrum is a method with higher resolution and is suitable for nonlinear and non-stationary signals. Yue et al. [49] applied the Hilbert marginal spectrum to analyse the stall and compared it with the Fourier transform to accurately identify the frequency of the stall signal.

Figure 17 shows the comparison between the Hilbert marginal spectrum and Fourier spectrum at the 180° circumferential position at 0.21kg/s. In order to distinguish the signals, the component below RF is called the low-frequency component, and the component between RF and BPF is called the high-frequency component. Generally, the low-frequency component signal represents the stall, while the high-frequency component signal represents the RI. For the high-frequency signal, it was also called high-frequency stall [55] or high-frequency pressure oscillation [56]. At 0.21kg/s, there are two distinct frequency components: 3 RF and 4.1 RF. However, there are multiple components in the Fourier spectrum, and it is difficult to determine which components are dominant in the origin signal. Compared to the Fourier frequency spectrum, the Hilbert marginal spectrum shows the dominant frequency except BPF, more clearly and has a better ability to analyse the instability signals. Although there are still many frequency components in the Hilbert marginal spectrum, they show the dominant frequencies more clearly to a great extent.

Figure 18 illustrates the comparison of the Hilbert marginal spectra of the 180° circumferential position at 0.21 and 0.20kg/s. At 0.20kg/s, the amplitude of the high-frequency components increases, and

https://doi.org/10.1017/aer.2022.31 Published online by Cambridge University Press

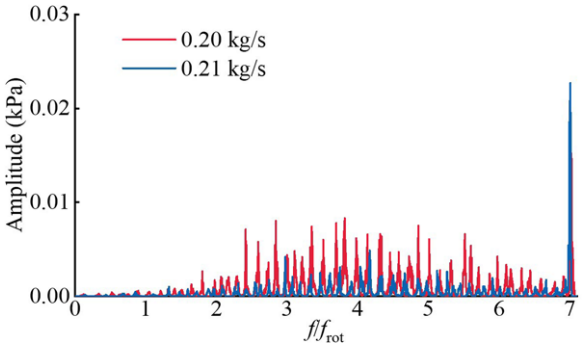

Figure 18. *Hilbert marginal spectrum at 180° circumferential position at 0.20kg/s, 80krpm.*

the amplitude of the BPF decreases significantly. This phenomenon indicates that compressor has gone into the RI state at 0.21kg/s and the RI is further enhanced at 0.20kg/s. In addition, it can also be observed that there are no significant low-frequency components at 0.21 and 0.20kg/s.

6.3.2 Evolution and circumferential nonuniformity characteristics of flow instability

Figure 19 shows the Hilbert marginal spectrum at different circumferential positions at 0.18, 0.16, 0.14, and 0.12kg/s. At 0.18kg/s, in addition to BPF, there is a broadband frequency hump composed of high-frequency components, representing the RI. The frequency band indicates that under this operating condition, RI is the primary type of instability. The broadband frequency hump of the RI is mainly concentrated between 2 RF and 5 RF. However, there is a small difference in the frequency spectrum characteristics at different circumferential positions. At the 180° circumferential position, the amplitude of the BPF is distinctly different from that of other circumferential positions. Compared with 0.20kg/s, the amplitude of the BPF significantly decreases, reaching a value lower than the maximum amplitude of the frequency band of the RI. Meanwhile, the RI amplitude increases significantly. On the other hand, at the 60°, 120°, 180°, and 240° circumferential position, there are low-frequency components, representing the stall occurrence. However, there is no obvious stall frequency at the 0° and 300° circumferential position. It can be concluded that the instability type of the compressor has an obvious circumferential nonuniformity. At this operating point, RI is the main instability phenomenon, whereas a slight stall occurs in the partial circumferential range.

At 0.16kg/s, in addition to BPF, the broadband frequency hump of RI is mainly concentrated between RF and 3 RF. Compared to the operating condition with a mass flow rate of 0.18kg/s, the broadband frequency hump moves from high frequency to low frequency, and the Hilbert marginal spectrum amplitude decreases significantly. At all circumferential positions, low-frequency stall frequencies were observed. In addition, the stall frequency at different circumferential positions has a noticeable circumferential nonuniformity. The amplitude of the stall frequency at 240° circumferential positions is larger than that of the RI. At this operating point, the most obvious feature is that the RI and stall coexist more clearly.

When the compressor operates at the mass flow rate of 0.14kg/s, it can be observed that the low-frequency components increase significantly, whereas the high-frequency components become very small. In the entire circumferential range, the amplitude of the low-frequency stall was greater than that of the high-frequency RI. At this operating point, the compressor instability was dominated by the low-frequency stall. The compressor enters the stall state completely.

When the mass flow further decreases to 0.12kg/s near the surge point, it can be observed that the low-frequency stall completely dominates, and the high-frequency components almost disappear in the entire circumferential positions. Meanwhile, it can be seen that the amplitude of BPF decreases. At the 180° circumferential position, the amplitude of the BPF is far less than that of the stall. The amplitude of the stall is almost the same as that of the BPF at the 240° circumferential position. It can be inferred

https://doi.org/10.1017/aer.2022.31 Published online by Cambridge University Press

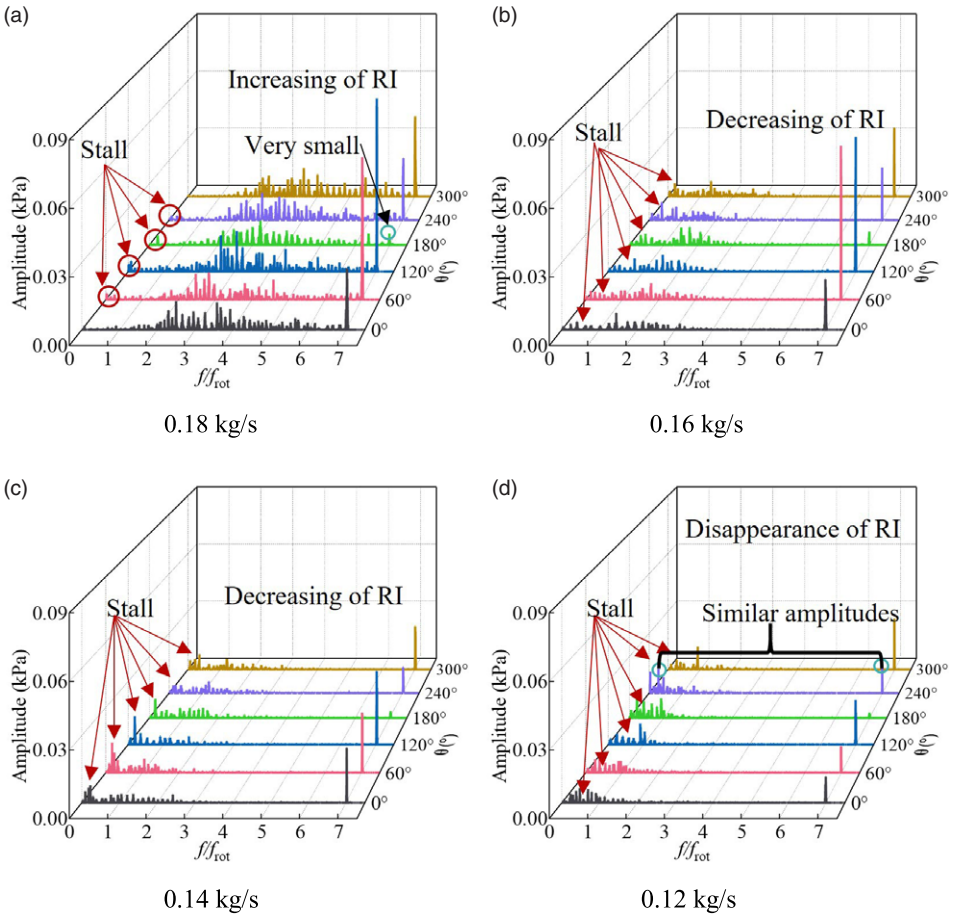

Figure 19. *Hilbert marginal spectrum at different circumferential positions at 80krpm.*

that if the mass flow further decreases, the amplitude of the BPF might be less than that of the stall. In the experiment, when the mass flow rate decreased further, the compressor quickly entered the surge state. It can be concluded that deep stall first occurs at these two positions, which is related to the impending surge. According to the experiments, the compressor surge may be triggered by a deep stall in the circumferential range of 180 to 240°.

Based on the above analysis, both the RI and stall exhibit circumferential nouniformity for the centrifugal compressor. At 0.21kg/s, the RI occurs in the entire circumferential range. At 0.18kg/s, the compressor first enters the stall condition in the circumferential range of 60° to 240°, while the other circumferential position still operates under the RI condition. As the mass flow rate decreases, the deep stall first occurs in the circumferential range of 120° to 240°. Generally, according to the above analysis, as the mass flow rate decreases, the instability process of the compressor can be summarised as follows: RI → RI & stall (coexistence stage) → stall (slight stall and deep stall) → surge. The process is clearly marked on the curve of the performance characteristics in Fig. 20.

7 Discussions

The cause of circumferential nouniformity of RI and stall was deeply explored by performing unsteady simulations at 0.26, 0.24, and 0.21kg/s (RI). The static pressure distribution of the casing wall is shown

https://doi.org/10.1017/aer.2022.31 Published online by Cambridge University Press

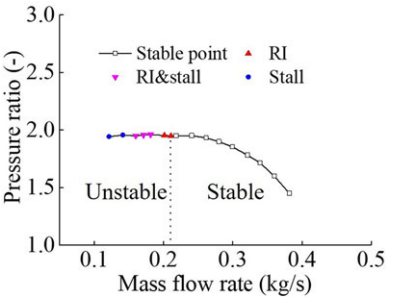

Figure 20. *Instability process at 80krpm.*

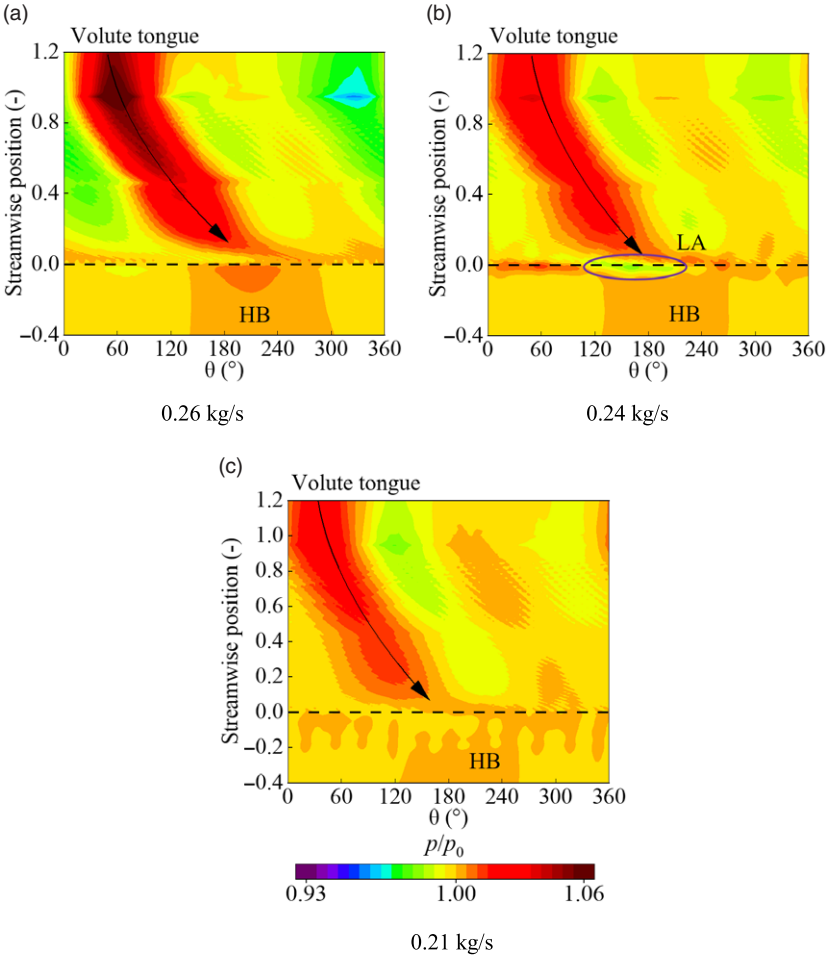

Figure 21. *Casing wall static pressure distributions at 80krpm.*

in Fig. 21. The dimensionless static pressure was obtained by dividing the static pressure by the circumferential average. The horizontal axis represents the circumferential angle, and the longitudinal axis represents the dimensionless streamwise position. In this figure, 0 and 1 represent the impeller inlet and outlet, respectively. Thus, the circumferentially nonuniform static pressure distribution is clearly indicated. A significant circumferential non-uniform distribution of the static pressure was observed around

https://doi.org/10.1017/aer.2022.31 Published online by Cambridge University Press

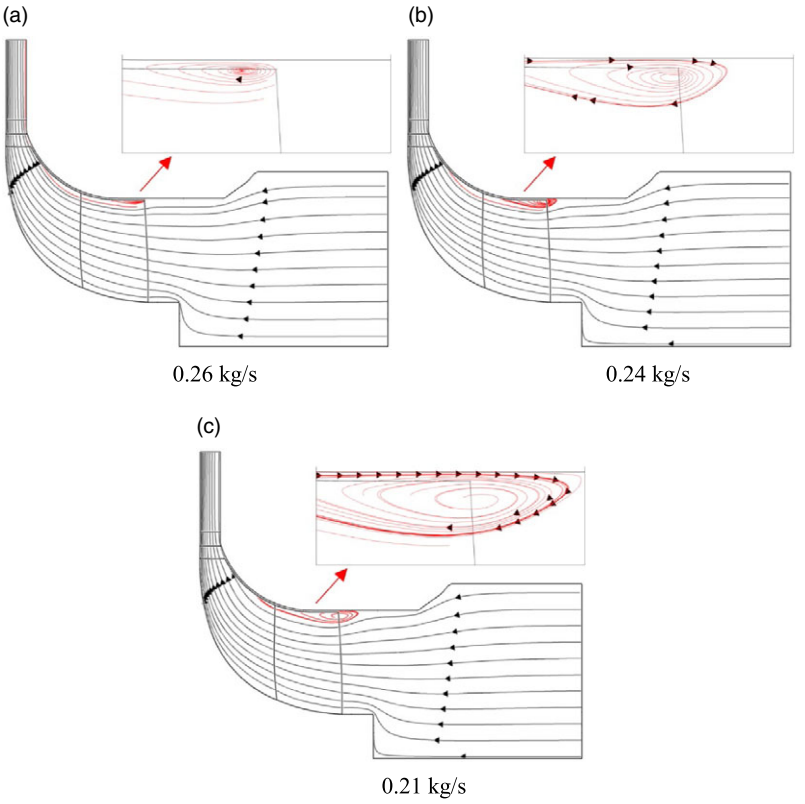

Figure 22. *Circumferential averaged streamline distribution of the compressor at 80krpm.*

the casing wall. This nonuniform distribution phenomenon could only be caused by the asymmetric structure of the volute tongue. Previous studies [57–59] have discussed the effect of the volute tongue on the static pressure distribution in a centrifugal compressor. The airflow is divided by the volute tongue and forced to recirculate around the volute at a low flow rate. Therefore, the volute tongue acts as a diffuser at a low mass flow rate, thereby forming a high static pressure region. Eventually, the volute tongue causes an adverse pressure wave. In Fig. 21, it can be observed that there is a high static pressure strip representing the pressure wave, marked with a black curve with an arrow. The high static pressure strip extends to the impeller inlet, resulting in a circumferentially nonuniform distribution at the inlet of the impeller. A high static pressure region HB is seen at the upstream of the impeller at these three operating points. The high-pressure region HB is approximately concentrated between 120° and 300°. This region is most affected by reverse pressure wave. As the mass flow rate decreases, at 0.24kg/s, a low-pressure region LA between 120° and 270° occurs near the LE of the blade. The low-pressure region LA results in a pressure decrease caused by the blade rotation, which is manifested as a significant decrease in the amplitude corresponding to the BPF, as shown in Fig. 13. At 0.21kg/s, some high-pressure spots occur upstream of the inlet. This indicates that the degree of circumferential nonuniformity becomes more obvious. The high-pressure region HB was concentrated between approximately 120° and 240°. Based on the analysis in Section 6.3, RI first occurs at this operating point. It can be concluded that increasing the circumferential nonuniformity leads to the occurrence of RI.

Figure 22 illustrates the movement of the tip leakage vortex at three different operating points. As the mass flow rate decreases, the rolling up of a shear layer between the tip leakage flow and the main flow forms a tip leakage vortex. At 0.26kg/s, the tip leakage vortex is located at the tip region near the impeller inlet. Under the action of the reverse pressure gradient, the tip leakage vortex moves to the inlet of the

https://doi.org/10.1017/aer.2022.31 Published online by Cambridge University Press

impeller passage. At 0.24kg/s, the vortex size increases; meanwhile, the reach of the vortex expands to the upstream of the impeller inlet, and the vortex core moves towards the blade leading edge. At this time, the low-pressure region LA is caused by the tip leakage vortex, as shown in Fig. 21. At 0.21kg/s, it can be seen that the vortex core migrates to the lower span and the reach of the vortex further extends upstream. During this period, RI first occurs at the 180° circumferential position in the compressor. This phenomenon indicates that the movement of the tip leakage vortex is closely related to the occurrence of the RI. If the mass flow rate further decreases, RI and stall just first occur in the high-pressure region HB caused by the volute tongue. With the further development of the stall, the 180° and 240° circumferential positions successively enter a deep stall, and finally, a surge occurs in the centrifugal compressor. Based on the above analysis, it can be summarised that the high static pressure region induced by the volute tongue determines the circumferential occurrence position of the RI and stall at the impeller inlet.

8 Conclusions

In this study, the evolution and circumferential nonuniformity characteristics of the flow instabilities in a centrifugal compressor with a volute were investigated based on dynamic pressure experiments. During the throttling process, six dynamic pressure sensors were installed evenly at the inlet of the compressor to obtain the dynamic pressure at the different circumferential positions. Both classical Fourier transform and advanced signal processing technique (VMD) were introduced to shed light on instability phenomena at 80krpm. The following conclusions were drawn:

(1) A Fourier transform was used to determine whether the compressor entered a state of instability. The VMD method and Hilbert marginal spectrum were applied to analyse the pressure signals under different instability conditions. Using this method, not only could the additional spurious harmonic components in the Fourier transform be avoided to the greatest extent, but also the frequency resolution for the nonlinear and non-stationary instability signals could be improved. This combined method can achieve better results when dealing with dynamic pressure signals.

(2) During the throttling process, the centrifugal compressor experienced different instability stages: RI stage, coexistence stage of RI and stall, and stall stage. In the RI stage (0.21–0.20kg/s), the Hilbert marginal spectrum amplitude gradually increased, which indicated that strength of RI gradually increased. In the coexistence stage of RI and stall (0.18–0.16kg/s), the Hilbert marginal spectrum amplitude of RI gradually decreased, and the corresponding broadband frequency hump moved from high to low frequency, which represented a gradual decrease in the RI strength. In this stage, the Hilbert marginal spectrum amplitude of the BPF at the 180° circumferential position was less than the maximum amplitude of the RI. In the stall stage (0.14–0.12kg/s), the RI almost disappeared. The compressor instability was dominated by low-frequency stall. Eventually, the compressor entered the surge state.

(3) During the throttling process, the instability process exhibited an obvious circumferential nonuniformity phenomenon in the centrifugal compressor. The RI first occurred at the 180° circumferential position. The stall first occurred in the circumferential range of 60°–240°. As the mass flow rate decreased, a stall occurred in the entire circumferential range. Compared to the other circumferential positions, the BPF amplitude decreased the most between 180° and 240°, which in turn triggered a surge.

(4) The initial occurrence position of the instability phenomena in the centrifugal compressor was determined by the asymmetric volute. The reverse pressure wave induced by the volute tongue led to a high static pressure region upstream of the impeller inlet. Under the combined action of the high static pressure region and reverse pressure gradient, the tip leakage vortex migrated to the inlet and the lower span. When the tip leakage vortex greatly exceeded the blade leading edge, it triggers instability.

https://doi.org/10.1017/aer.2022.31 Published online by Cambridge University Press

Acknowledgments. This work was supported by the National Natural Science Foundation of China (Grant No. 51736001) and was undertaken at the Turbomachinery Institute under the Beijing Institute of Technology, China.

Declaration of competing interest. The authors have no conflict of interest declare.

References

[1] McDougall, N.M., Cumpsty, N.A. and Hynes, T.P. Stall inception in axial compressors, *J Turbomach*, 1990, **112**, pp 116–123. doi: 10.1115/1.2927406.
[2] Day, I.J. Stall inception in axial flow compressors, *J Turbomach*, 1993, **115**, pp 1–9. doi: 10.1115/1.2929209.
[3] Greitzer, E.M. Surge and rotating stall in axial flow compressors—Part II: Experimental results and comparison with theory, *J Eng Power*, 1976, **98**, pp 199–211. doi: 10.1115/1.3446139.
[4] Liu, Y., Li, J., Du, J., Li, F. and Zhang, H. Application of fast wavelet analysis on early stall warning in axial compressors, *J Therm Sci*, 2019, **28**, pp 837–849.
[5] Arshad, .A., Li, Q., Li, S. and Pan, T. Effects of inlet radial distortion on the type of stall precursor in low-speed axial compressor, *Proc Inst Mech Eng Part G J Aerosp Eng*, 2016, **232**, pp 55–67. doi: 10.1177/0954410016670679.
[6] Vo, H.D., Tan, C.S. and Greitzer, E.M. Criteria for spike initiated rotating stall, *J Turbomach*, 2008, **130**. doi: 10.1115/1.2750674.
[7] Spakovszky, Z.S. and Roduner, C.H. Spike and modal stall inception in an advanced turbocharger centrifugal compressor, *J Turbomach*, 2009, **131**, pp 1745–1755. https://doi.org/10.1115/1.2988166.
[8] Everitt, J.N. and Spakovszky, Z.S. An investigation of stall inception in centrifugal compressor vaned diffuser, *J Turbomach*, 2012, **135**. doi: 10.1115/1.4006533.
[9] Bousquet, Y., Binder, N., Dufour, G., Carbonneau, X., Trebinjac, I. and Roumeas, M. Numerical investigation of Kelvin-Helmholtz instability in a centrifugal compressor operating near stall, *J Turbomach*, 2016, **138**. doi: 10.1115/1.4032457.
[10] Bousquet, Y., Binder, N., Dufour, G., Carbonneau, X., Trebinjac, I., Roumeas, M., Numerical investigation of Kelvin-Helmholtz instability in a centrifugal compressor operating near stall, *J Turbomach*, 2016, **138**. doi: 10.1115/1.4032457.
[11] Yang, C., Wang, Y., Lao, D., Wang, W., Yang, C., Chen, X. and Zhang, H. Detailed measurements of the static pressure characteristics around the centrifugal compressor casing wall, *J Therm Sci Technol*, 2017, **12**, pp JTST0009–JTST0009. doi: 10.1299/jtst.2017jtst0009.
[12] Yang, C., Wang, Y., Tong, D., Yang, C. and Li, Y. Stall inception induced by the volute tongue at centrifugal compressor inlet, *Proc Inst Mech Eng Part G J Aerosp Eng*, 2017, **231**, pp. 931–940. doi: 10.1177/0954410016645127.
[13] Yang, C., Zhang, H., Yang, D., Lao, D. and Yang, C. Casing wall static pressure distribution behavior in a centrifugal compressor with asymmetric inlet/outlet structures, *Proc Inst Mech Eng Part A J Power Energy*, 2019, **233**, pp. 37–51. doi: 10.1177/0957650918774934.
[14] Zhang, H., Yang, C., Yang, C., Zhang, H., Wang, L. and Chen, J., Inlet bent torsional pipe effect on the performance and stability of a centrifugal compressor with volute, *Aerosp Sci Technol*, 2019, **93**, p 105322. doi: 10.1016/j.ast.2019.105322.
[15] Kameier, F. and Neise, W. Rotating blade flow instability as a source of noise in axial turbomachines, *J Sound Vib*, 1997, **203**, pp. 833–853. doi: 10.1006/jsvi.1997.0902.
[16] Kameier, F. and Neise, W. Experimental study of tip clearance losses and noise in axial turbomachines and their reduction, *J Turbomach*, 1997, **119**, pp 460–471. doi: 10.1115/1.2841145.
[17] Mailach, R., Lehmann, I. and Vogeler, K. Rotating instabilities in an axial compressor originating from the fluctuating blade tip vortex, *J Turbomach*, 2000, **123**, pp 453–460. doi: 10.1115/1.1370160.
[18] Mailach, R., Sauer, H. and Vogeler, K. The periodical interaction of the tip clearance flow in the blade rows of axial compressors, ASME Turbo Expo 2001 Power Land, Sea, Air. (2001). doi: 10.1115/2001-GT-0299.
[19] Vo, H.D. Role of tip clearance flow in rotating instabilities and nonsynchronous vibrations, *J Propuls Power*, 2010, **26**, pp 556–561. doi: 10.2514/1.26709.
[20] Sun, Z., Zou, W. and Zheng, X. Instability detection of centrifugal compressors by means of acoustic measurements, *Aerosp Sci Technol*, 2018, **82–83**, pp 628–635. doi: 10.1016/j.ast.2018.09.006.
[21] Li, T., Wu, Y. and Ouyang, H. Influence of axial skewed slots on the rotating instability of a low-speed axial compressor, *Proc Inst Mech Eng Part G J Aerosp Eng*, 2020, **235**, pp 385–401. doi: 10.1177/0954410020944331.
[22] Li, T., Wu, Y. and Ouyang, H. Numerical investigation of tip clearance effects on rotating instability of a low-speed compressor, *Aerosp Sci Technol*, 2021, **111**, p 106540. doi: 10.1016/j.ast.2021.106540.
[23] Ye, S., Zhao, Q., Zhou, X., Xi, G. and Xu, J. The impact of circumferential casing grooves on rotating instability in a transonic axial compressor, *Proc Inst Mech Eng Part G J Aerosp Eng*, 2018, **233**, pp 2868–2893. doi: 10.1177/0954410018786094.
[24] Zou, W., He, X., Zhang, W., Niu, Z. and Zheng, X. Roles of vanes in diffuser on stability of centrifugal compressor, *Proc Inst Mech Eng Part G J Aerosp Eng*, 2019, **233**, 5380–5392. doi: 10.1177/0954410019844433.
[25] He, X. and Zheng, X. Roles and mechanisms of casing treatment on different scales of flow instability in high pressure ratio centrifugal compressors, *Aerosp Sci Technol*, 2019, **84**, pp 734–746. doi: 10.1016/j.ast.2018.10.015.
[26] Wang, Z., Lu, B., Liu, J. and Hu, J. Numerical simulation of unsteady tip clearance flow in a transonic compressor rotor, *Aerosp Sci Technol*, 2018, **72**, pp 193–203. doi: 10.1016/j.ast.2017.11.012.
[27] Holzinger, F., Wartzek, F., Schiffer, H.-P., Leichtfuss, S. and Nestle, M. Self-excited blade vibration experimentally investigated in transonic compressors: Acoustic resonance, *J Turbomach*, 2015, **138**. doi: 10.1115/1.4032042.

[28] Wu, Y., An, G. and Wang, B. Numerical investigation into the underlying mechanism connecting the vortex breakdown to the flow unsteadiness in a transonic compressor rotor, *Aerosp Sci Technol*, 2019, **86**, pp 106–118. doi:https://doi.org/10.1016/j.ast.2018.12.040.

[29] Eck, M., Rückert, R., Peitsch, D. and Lehmann, M. Prestall instability in axial flow compressors, *J Turbomach*, 2020, **142**. doi: 10.1115/1.4046447.

[30] Wang, W., Yang, C., Hu, C. and Zhang, H. Investigation of tip leakage flow unsteadiness and rotating instability in a centrifugal compressor impeller, *Proc Inst Mech Eng Part D J Automob Eng*, 2021, 09544070211025902. doi: 10.1177/09544070211025902.

[31] Lin, F., Chen, J. and Li, M. Wavelet analysis of rotor-tip disturbances in an axial-flow compressor, *J Propuls Power*, 2004, **20**, pp 319–334. doi: 10.2514/1.9257.

[32] Lin, F., Li, M. and Chen, J. Long-to-short length-scale transition: A stall inception phenomenon in an axial compressor with inlet distortion, *J Turbomach*, 2005, **128**, pp 130–140. doi: 10.1115/1.2098808.

[33] Cameron, J.D. and Morris, S.C. Analysis of axial compressor stall inception using unsteady casing pressure measurements, *J Turbomach*, 2012, **135**. doi: 10.1115/1.4006777.

[34] Toge, T.D. and Pradeep, A.M. Experimental investigation of stall inception of a low speed contra rotating axial flow fan under circumferential distorted flow condition, *Aerosp Sci Technol*, 2017, **70**, pp 534–548. doi: 10.1016/j.ast.2017.08.041.

[35] Dejene Toge, T. and Pradeep, A.M. Experimental investigation of stall inception mechanisms of low speed contra rotating axial flow fan stage, *Int J Rotating Mach*, 2015, 2015, p 641601. doi: 10.1155/2015/641601.

[36] Liu, Y., Li, J., Du, J., Zhang, H. and Nie, C. Reliability analysis for stall warning methods in an axial flow compressor, *Aerosp Sci Technol*, 2021, **115**, p. 106816. doi: 10.1016/j.ast.2021.106816.

[37] Niccolini Marmont Du Haut Champ, C.A., Ferrari, M.L., Silvestri, P. and Massardo, A.F. Signal processing techniques to detect centrifugal compressors instabilities in large volume power plants, ASME Turbo Expo 2020 Turbomach. Tech. Conf. Expo. (2020). doi: 10.1115/GT2020-14795.

[38] Li, H., Zheng, Q., Chen, Z., Duan, Y., Jiang, B. and Benini, E. The role of radial secondary flow in the process of rotating stall for a 1.5-stage axial compressor, *Aerosp Sci Technol*, 2021, **115**, p. 106752. doi: 10.1016/j.ast.2021.106752.

[39] Li, J., Du, J., Liu, Y., Zhang, H. and Nie, C. Effect of inlet radial distortion on aerodynamic stability in a multi-stage axial flow compressor, *Aerosp Sci Technol*, 2020, **105**, p. 105886. doi: 10.1016/j.ast.2020.105886.

[40] Manas, M.P. and Pradeep, A.M. Stall inception in a contra-rotating fan under radially distorted inflows, *Aerosp Sci Technol*, 2020, **105**, p 105909. doi: 10.1016/j.ast.2020.105909.

[41] Manas, M.P. and Pradeep, A.M. Stall inception mechanisms in a contra-rotating fan operating at different speed combinations, *Proc Inst Mech Eng Part A J Power Energy*, 2019, **234**, pp 1041–1052. doi: 10.1177/0957650919893831.

[42] Wang, J., Chen, J., Dong, G. and Hua, H. Wavelet features and hidden Markov model-based aerodynamic instability detection for compressors, *J Turbomach*, 2019, **141**. doi: 10.1115/1.4044495.

[43] Huang, N.E., Shen, Z., Long, S.R., Wu, M.C., Shih, H.H., Zheng, Q., Yen, N.-C., Tung, C.C. and Liu, H.H. The empirical mode decomposition and the Hilbert spectrum for nonlinear and non-stationary time series analysis, *Proc Math Phys Eng Sci*, 1998, **454**, pp 903–995. http://www.jstor.org/stable/53161.

[44] Li, C., Lei, Y. and Fu, R. Aerodynamic instability detection in compressor based on Hilbert-Huang transform, 2011 IEEE International Conference on Computer Science and Automation Engineering, 2011, pp 355–358. doi: 10.1109/CSAE.2011.5952867.

[45] Wu, X., Liu, Y., Liu, R. and Zhao, L. Surge detection methods using empirical mode decomposition and continuous wavelet transform for a centrifugal compressor, *J Mech Sci Technol*, 2016, **30**, pp 1533–1536. doi: 10.1007/s12206-016-0307-2.

[46] Zhao, J., Xi, G., Wang, Z. and Zhao, Y. The unsteady pre-stall behavior of the spike-type rotating stall within an airfoil Vaned-diffuser, ASME Turbo Expo 2018 Turbomach. Tech. Conf. Expo., 2018. doi: 10.1115/GT2018-76145.

[47] Liu, Y., Ma, K., He, H. and Gao, K. Obtaining information about operation of centrifugal compressor from pressure by combining EEMD and IMFE, *Entropy*, 2020, **22**. doi: 10.3390/e22040424.

[48] Guan, D., Sun, D., Xu, R., Bishop, D., Sun, X., Ni, S., Du, J. and Zhao, D. Experimental investigation on axial compressor stall phenomena using aeroacoustics measurements via empirical mode and proper orthogonal decomposition methods, *Aerosp Sci Technol*, 2021, **112**, p. 106655. doi: 10.1016/j.ast.2021.106655.

[49] Yue, S., Wang, Y., Wei, L., Zhang, Z. and Wang, H. The joint empirical mode decomposition-local mean decomposition method and its application to time series of compressor stall process, *Aerosp Sci Technol*, 2020, **105**, p. 105969. doi: 10.1016/j.ast.2020.105969.

[50] Dragomiretskiy, K. and Zosso, D. Variational mode decomposition, *IEEE Trans Signal Process*, 2014, **62**, pp 531–544. doi: 10.1109/TSP.2013.2288675.

[51] Hu, C., Yang, C., Yi, W., Zheng, S., Zou, R. and Zhou, M. Influence of shroud profiling on the compressor diffuser: Frozen-eddy approach and mode decomposition, *Int J Mech Sci*, 2020, **178**, p 105623. doi: 10.1016/j.ijmecsci.2020.105623.

[52] Yang, C., Fu, L., Hu, C. and Shi, X. Modelling and dynamic mode analysis of compressor impeller spike-type stall with global stability approach, *Int J Mech Sci*, 2021, **201**, p. 106486. doi: 10.1016/j.ijmecsci.2021.106486.

[53] Dodds, J. and Vahdati, M. Rotating stall observations in a high speed compressor—Part II: Numerical study, *J Turbomach*, **137**, 2015. doi: 10.1115/1.4028558.

[54] Pullan, G., Young, A.M., Day, I.J., Greitzer, E.M. and Spakovszky, Z.S. Origins and structure of spike-type rotating stall, *J Turbomach*., 2015, **137**. doi: 10.1115/1.4028494.

[55] Zheng, X. and Liu, A. Experimental investigation of surge and stall in a high-speed centrifugal compressor, *J Propuls Power*, 2015, **31**, pp 815–825. doi: 10.2514/1.B35448.

https://doi.org/10.1017/aer.2022.31 Published online by Cambridge University Press

[56] Zheng, X., Sun, Z., Kawakubo, T. and Tamaki, H. Experimental investigation of surge and stall in a turbocharger centrifugal compressor with a Vaned diffuser, *Exp Therm Fluid Sci*, 2017, **82**, pp 493–506. doi: 10.1016/j.expthermflusci.2016.11.036.
[57] Yang, C., Wang, Y., Tong, D., Yang, C. and Li, Y. Stall inception induced by the volute tongue at centrifugal compressor inlet, *Proc Inst Mech Eng Part G J Aerosp Eng*, 2016, **231**, pp 931–940. doi: 10.1177/0954410016645127.
[58] Yang, C., Wang, W., Zhang, H., Yang, C. and Li, Y. Investigation of stall process flow field in transonic centrifugal compressor with volute, *Aerosp Sci Technol*, 2018, **81**, pp 53–64. doi: 10.1016/j.ast.2018.07.047.
[59] Zhang, H., Yang, C., Wang, W., Chen, J. and Qi, M. Investigation on the casing static pressure distribution and stall behaviors in a centrifugal compressor with volute, *Int J Mech Sci*, 2019, **160**, pp 318–331. doi: 10.1016/j.ijmecsci.2019.06.043.

Cite this article: Wang W., Zhang H., Yang C., Yang C. and Hu C. (2022). Experimental analysis of flow instability detection in a centrifugal compressor using variational mode decomposition. *The Aeronautical Journal*, **126**, 2058–2082. https://doi.org/10.1017/aer.2022.31